Identification and Control of LCC-S WPT Systems Using a Linear Parameter Varying Model

Yuchen Feng, *Student Member, IEEE*, Fengwei Chen, Yue Sun, Tao Lin, Fanbin Meng, *Student Member, IEEE*, and Hongsheng Hu, *Member, IEEE*

***Abstract*—In this article, the problem of modeling and control of an LCC-S wireless power transfer (WPT) system in the presence of rectifier discontinuous conduction and load variation is considered. The diode bridge in an LCC-S WPT system often enters the discontinuous conduction mode (DCM), due to its unidirectional conductivity property. To better handle this type of nonlinearity, a linear parameter varying (LPV) model, which allows the model parameters to change with respect to a set of chosen dependence variables, is suggested to describe the dynamic behavior of the system. Based on this LPV model, a modified two degrees of freedom internal model control structure is proposed. The proposed control structure can switch between open loop and closed loop: when the system is in DCM, the system is configured as open loop because the load voltage or current is uncontrollable from the primary side, where any control action may impair the control system performance; otherwise, the system is operated in closed loop. Experimental results are provided to validate the effectiveness of the proposed modeling and control method.**

***Index Terms*—Discontinuous conduction mode, internal model control, linear parameter varying model, wireless power transfer.**

I. Introduction

As A convenient, flexible, safe, and efficient power transfer technology, magnetically coupled wireless power transfer (WPT) technology can help the electrical appliances get rid of the shackle of the wire, and has a broad application prospect [1], [2], [3], [4], [5], [6], [7], [8], [9], [10], [11]. To improve the application efficiency of the WPT system, scholars have done a lot of research on coupling structure design [12], [13], [14], resonance topology [15], [16], [17], frequency characteristic analysis [18], [19], [20], etc. As an effective means to improve the safety, reliability, and economy of WPT systems, modeling and control [21] has attracted much attention in recent years.

Normally, the first step in control design is to establish a suitable system model. The WPT system is a high-order and nonlinear system due to the high-frequency resonant networks, the inverter, and the rectifier in the primary and secondary side circuits. The switching nature of the inverter and rectifier brings difficulties to the accurate modeling of the WPT system. At present, a popular modeling method is generalized state-space averaging (GSSA) [22], [23], [24], [25]. Any ac state variable in the system can be represented via Fourier series as long as it satisfies the Dirichli condition. Then, the general state equation of the system can be obtained by substituting the state variable represented by the Fourier series into the state space equation. By ignoring the high order harmonics of the state variables, the required accuracy can be achieved. The disadvantage of this method is that the model order is high, which makes the controller more complicated.

Aiming at the problems of high order and complex frequency domain analysis of system models built by methods such as GSSA, scholars have carried out relevant research on model order reduction [26], [27]. In [28], the authors removed the poles that are less important to control system design by inspecting the Bode diagram, and obtain a reduced-order model of the system to analyze the low-frequency characteristics. According to the principle of GSSA and other methods, e.g., [26], the reason for obtaining a high-order model is that the system state variable is characterized by two independent parameters, namely amplitude and phase. Therefore, a circuit simplification method based on phasor transform is proposed, which decomposes the inductive components into frequency-dependent and frequency-independent parts. The inductor is equivalent to two parts in series, and the capacitor is equivalent to two parts in parallel. By combining the equivalent components, the two components can be equivalent to one component, thereby simplifying the model and reducing the model order. In [29], a general polynomial approximation technique is proposed to model the system with low order. The principle is related to the state variables in a differential equation built according to the circuit principle. Through the Taylor series expansion of different orders of the variables on both sides of the equation, a simplified model of the system can be obtained. According to the requirements of accuracy, the Taylor series can be expanded to the required order. Through Bode diagram, it is found that the low frequency band characteristics of the system can be described by a low-order model, and the characteristics used are similar to those in [28], but the modeling process and expression are more general.

As regards controller design, a PID parameter tuning method based on genetic algorithm for high-order system such as bidirectional WPT system is discussed in [30]. The parameters

Manuscript received 19 January 2024; revised 7 May 2024; accepted 7 June 2024. Date of publication 17 June 2024; date of current version 16 July 2024. This work was supported in part by the National Natural Science Foundation of China under Grant 62073246, Grant 62073047, and Grant 52207003. Recommended for publication by Associate Editor Mario Ponce-Silva. *(Corresponding author: Fengwei Chen.)*

The authors are with the School of Automation, Chongqing University, Chongqing 400044, China (e-mail: fengyuchen@cqu.edu.cn; fengwei.chen@cqu.edu.cn; syue06@cqu.edu.cn; 20211301005@stu.cqu.edu.cn; 202213021063t@stu.cqu.edu.cn; huhongsheng@cqu.edu.cn).

Color versions of one or more figures in this article are available at https://doi.org/10.1109/TPEL.2024.3415056.

Digital Object Identifier 10.1109/TPEL.2024.3415056

of the PID controller are determined using a multiobjective genetic algorithm by properly selecting the objective function, which is a weighted combination of settling time, rising time, and peak overshoot. Compared with the traditional PID controller, it has better robustness and stability, but it also has higher computing burden. Model predictive Control (MPC) is used in [31] to ensure the optimal dynamic tracking performance of the system when the coupling coefficient changes rapidly in a wide range. The GSSA method is used in [32] to establish a linear model for the system and designs an H_∞ controller to eliminate the external disturbance and parameter disturbance. However, the precondition of the method proposed in [31] and [32] is that all circuit parameters of the system can be accurately measured.

It is noticed that when the induced voltage at the input port of the rectifier is lower than the load voltage, the rectifier will enter the discontinuous conduction mode (DCM) [33]. In this state, no current flows through the diode bridge, indicating that the state of the secondary side of the system cannot be controlled from the primary side, which poses a great challenge to control design. Moreover, the problem on how to improve the quality of control in DCM has been seldom investigated in the literature. In this article, the internal model control (IMC, see, e.g., [34], [35]) with configurable structure is proposed. That is, the system is configured in the open-loop control mode if DCM is detected, otherwise the system remains in the closed-loop control mode. Moreover, to improve the accuracy of system modeling that is helpful for control design, this article adopts the linear parameter varying (LPV) modeling method in [36], in which the structure and parameters of the model are obtained only through the experimental data regardless of the detailed circuit parameters. Compared with the full closed-loop control strategy, since DCM has been fully considered in modeling and control in the proposed strategy, the modeling accuracy can be improved by the LPV model, and the control quality can be improved by the mode switching control strategy. The rectifier is a common nonlinear device in ac–dc power conversion, whose nonlinearity primarily arises from the parasitic properties of the rectification diode and the line-commutation process [37], [38]. The influence of the input impedance of rectifiers was discussed in [39], where the impedance was obtained from the PSPICE model, but the generalization of this model to other devices has not been discussed. In [40], by disregarding the nonlinearity caused by the line commutation process, an analytical model for the impedance of rectifiers in positive half cycle was introduced. In [41], a measurement-based characterization method for rectifiers is proposed, where curve-fitting techniques such as polynomials and rational functions were proposed to approximate the behavior of a rectifier. Nevertheless, this approach is unsuitable for systems operating above the MHz frequency range. An accurate load model for nonlinear rectifiers was established in [42], which takes the current interruption and parasitic parameters into account, thus enabling accurate handling of all load conditions with continuous or discontinuous rectifier currents. However, due to the presence of input reactance, this model is also unsuitable for systems operating above the MHz frequency range.

The rest of this article is organized as follows: The model of the WPT system under consideration is analyzed in Section II; The control system design based on the resulting model is discussed in Section III; Subsequently, experimental results are given in Section IV to validate the modeling and control methods; Finally, conclusions are drawn in Section V.

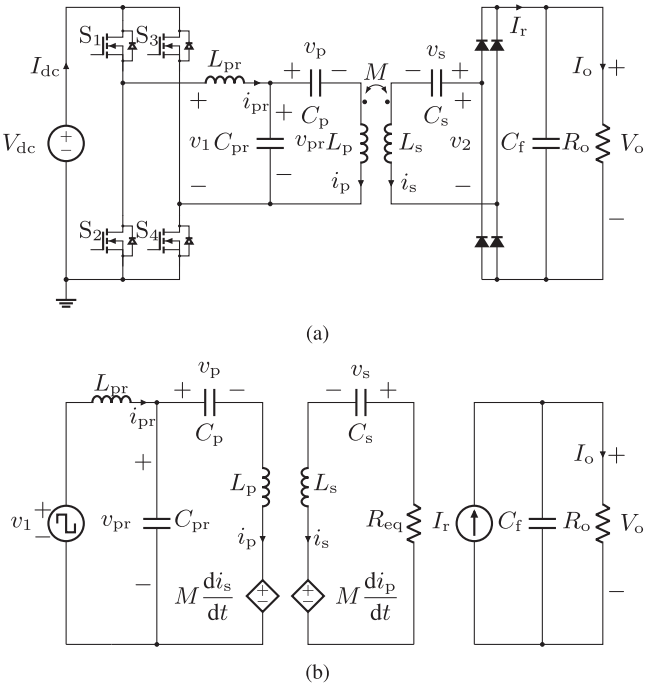

Fig. 1. LCC-S WPT system. (a) Circuit diagram. (b) Equivalent circuit.

II. Control-Oriented Modeling

The identification and control method will be derived on the basis of the LCC-S WPT system described in Fig. 1(a), where the phase shift of the full-bridge inverter U is chosen as the control variable to regulate the load voltage V_o or current I_o. The primary side adopts an LCC compensation network composed of L_{pr}, C_{pr}, and C_p. The LCC compensation network is a parallel resonant converter, where the voltage of C_{pr} is used to transfer power from the source to the secondary side [43]. The secondary side takes a series compensation network using a single capacitor C_s. The LCC-S WPT system has an advantage that it acts like a voltage source and, so, the load voltage V_o is nearly independent of the load resistance R_o.

A. Model Structure Analysis

A model that relates the input and output variables of the WPT system is quite helpful for control design. Also, it is expected that the model is simple, with only a minimal number of parameters, but can accurately describe the dynamic behavior of the system. In this section, we explain how to derive the structure of this control-oriented model based on circuit theory. To facilitate this structural analysis process, it is assumed that switches and diodes in the circuit are considered as ideal, and that all the parasitic parameters are negligible. Under these assumptions, an equivalent circuit of the system in Fig. 1(a) can be derived;

see Fig. 1(b), where $R_{\rm eq}$ is the equivalent resistance of the rectifier load. Based on this equivalent circuit, by introducing the differential operator p: $p = d/dt$, the system can be described by the following equations:

$$\left(L_{\rm pr}p + \frac{1}{C_{\rm pr}p}\right)(i_{\rm pr} - i_{\rm p}) + L_{\rm pr}pi_{\rm p} = v_1 \tag{1a}$$

$$\left(L_{\rm p}p + \frac{1}{C_{\rm p}p}\right)i_{\rm p} + Mpi_{\rm s} = \frac{1}{C_{\rm pr}p}(i_{\rm pr} - i_{\rm p}) \tag{1b}$$

$$\left(L_{\rm s}p + \frac{1}{C_{\rm s}p} + R_{\rm eq}\right)i_{\rm s} + Mpi_{\rm p} = 0 \tag{1c}$$

$$(C_{\rm f}p + 1/R_{\rm o})\,V_{\rm o} = I_{\rm r}. \tag{1d}$$

In the above model, $I_{\rm r}$ and $i_{\rm s}$ are linked through

$$I_{\rm r} = \frac{1}{T_0}\int_0^{T_0} |i_{\rm s}|dt \tag{2}$$

where T_0 is the switching period and $|i_{\rm s}|$ denotes the absolute value of $i_{\rm s}$. Moreover, the variables $i_{\rm pr}$ and $i_{\rm p}$ can be eliminated from the first three equations of (1) to obtain a more compact model relating only $i_{\rm s}$ and v_1

$$\left(\left(Z_{\rm pr}(p)Z_{\rm p}(p) + \frac{L_{\rm pr}p^2}{C_{\rm pr}}\right)(Z_{\rm s}(p) + R_{\rm eq}p) - Z_{\rm pr}(p)M^2p^4\right)i_{\rm s} = -\frac{Mp^3}{C_{\rm pr}}v_1 \tag{3}$$

where $Z_{\rm pr}(p) = L_{\rm pr}p^2 + 1/C_{\rm pr}$; $Z_{\rm p}(p)$ and $Z_{\rm s}(p)$ are similarly defined.

Thanks to the good band-pass filtering feature of the resonant tank, it is reasonable to approximate $i_{\rm s}$ by its first harmonic in the following way:

$$i_{\rm s} \approx {\rm Re}\left\{I_{\rm s}{\rm e}^{j\omega_0 t}\right\} \tag{4}$$

where ω_0 is the angular switching frequency; $I_{\rm s} = I_{\rm sd} + jI_{\rm sq}$ is the complex-valued envelope of $i_{\rm s}$; $I_{\rm sd}$ and $I_{\rm sq}$ denote the real and imaginary parts of $I_{\rm s}$, respectively. In the same light, v_1 can be approximated as

$$\begin{aligned} v_1 &\approx {\rm Re}\left\{\frac{2}{\pi}V_{\rm dc}{\rm e}^{j\omega_0 t + U/2} - \frac{2}{\pi}V_{\rm dc}{\rm e}^{j\omega_0 t + \pi - U/2}\right\} \\ &= {\rm Re}\left\{\frac{4}{\pi}V_{\rm dc}\cos(U/2){\rm e}^{j\omega_0 t}\right\}. \end{aligned} \tag{5}$$

For the right-hand side of (4), it can be shown that (see also [36])

$$p^k\left\{I_{\rm s}{\rm e}^{j\omega_0 t}\right\} = (p + j\omega_0)^k\, I_{\rm s}{\rm e}^{j\omega_0 t},\ k \in \mathbb{N}. \tag{6}$$

Substituting (4)–(6) into (3) and eliminating ${\rm e}^{j\omega_0 t}$ from both sides, we have

$$\mathcal{A}(p)I_{\rm s} = \mathcal{B}(p)\cos(U/2) \tag{7a}$$

$$(C_{\rm f}p + 1/R_{\rm o})\,V_{\rm o} = I_{\rm r} \tag{7b}$$

where $\mathcal{A}(p)$ and $\mathcal{B}(p)$ are polynomials in p defined as

$$\begin{aligned} \mathcal{A}(p) = &(Z_{\rm pr}(p + j\omega_0)\cdot Z_{\rm p}(p + j\omega_0) \\ &+ L_{\rm pr}/C_{\rm pr}\cdot(p + j\omega_0)^2) \\ &\cdot (Z_{\rm s}(p + j\omega_0) + R_{\rm eq}\cdot(p + j\omega_0)) \\ &- Z_{\rm pr}(p + j\omega_0)\cdot M^2\cdot(p + j\omega_0)^4 \end{aligned} \tag{8a}$$

$$\mathcal{B}(p) = \frac{MV_1}{C_{\rm pr}}\cdot(p + j\omega_0)^3 \tag{8b}$$

in which $V_1 = 4V_{\rm dc}/\pi$.

It should be noted that the rectifier input voltage v_2 is a square wave of amplitude switching between $\pm V_{\rm o}$, so the amplitude of the first harmonic of v_2 is $4V_{\rm o}/\pi$. Then, $R_{\rm eq}$ is approximated as

$$R_{\rm eq} \approx \frac{4V_{\rm o}}{\pi|I_{\rm s}|}. \tag{9}$$

Furthermore, $i_{\rm s}$ is almost sinusoidal, so $I_{\rm r}$ can be approximated as

$$\begin{aligned} I_{\rm r} &= \frac{1}{T_0}\int_0^{T_0}|i_{\rm s}|dt \\ &\approx \frac{1}{T_0}\int_0^{T_0}|I_{\rm sd}\cos(\omega_0 t) - I_{\rm sq}\sin(\omega_0 t)|dt \\ &= \frac{2}{\pi}|I_{\rm s}|. \end{aligned} \tag{10}$$

The model (7) is composed of a sixth-order complex-valued part (7a) and a first-order real-valued part (7b). If the real and imaginary decomposition of (7a) is performed, the complete model will be converted to a real-valued model of order 13, which is too high. In the next section, we will use an LPV model instead of (7) for control-oriented modeling.

B. LPV Models

An LPV model adopts a linear model structure, but its parameters can vary as a function of the scheduling variables. In the LCC-S WPT system considered in this article, both $R_{\rm eq}$ and $R_{\rm o}$ could change. As shown in (7), the characteristic polynomial of (7a) is dependent on $R_{\rm eq}$ while the characteristic polynomial of (7b) is dependent on $1/R_{\rm o}$, so the characteristic polynomial of the LPV model that relates U and $V_{\rm o}$ could possibly be dependent on $R_{\rm eq}$, $1/R_{\rm o}$, and $R_{\rm eq}/R_{\rm o}$. Without any loss of generality, the LPV model to describe the system dynamics is defined as

$$A(p, h_1, h_2, h_3)V_{\rm o} = B(p)f(U) \tag{11}$$

where $h_1 = R_{\rm eq}$, $h_2 = 1/R_{\rm o}$, and $h_3 = R_{\rm eq}/R_{\rm o}$ are also called scheduling variables from here on, and

$$B(p) = \sum_{i=0}^{n_b} b_i p^{n_b - i} \tag{12a}$$

$$A\,(p, h_1, h_2, h_3) = p^{n_a} + \sum_{i=1}^{n_a}\left(a_{i,0} + \sum_{\ell=1}^{n_h} a_{i,\ell}r_\ell\right)p^{n_a - i} \tag{12b}$$

with $f(U)$ being the input nonlinearity function defined by

$$f(U) = \cos(U/2) + c \tag{13}$$

where c is an unknown parameter to be estimated.

In the above LPV model, each parameter is dependent on three scheduling variables h_1, h_2, and h_3, which increases for sure the model complexity. In the following, we will show how the number of dependencies can be reduced when information about the topology and parameter design of the system is taken into account. In the LCC-S WPT system, the circuit component parameters are selected such that

$$\omega_0 L_{\rm pr} = \frac{1}{\omega_0 C_{\rm pr}} = \omega_0 L_{\rm p} - \frac{1}{\omega_0 C_{\rm p}} \tag{14a}$$

$$\omega_0 L_{\rm p} = \omega_0 L_{\rm pr} + \frac{1}{\omega_0 C_{\rm p}} \tag{14b}$$

$$\omega_0 L_{\rm s} = \frac{1}{\omega_0 C_{\rm s}}. \tag{14c}$$

In this case, by replacing p in (7) by the Laplace operator s, the steady-state value of $I_{\rm s}$ can be obtained at $s \to 0$ as

$$\overline{I}_{\rm s} = \lim_{s\to 0} \frac{\mathcal{B}(s)}{\mathcal{A}(s)} f(U) = \frac{MV_1}{L_{\rm pr} R_{\rm eq}} f(U) \tag{15}$$

where it is shown that $\overline{I}_{\rm s}$ is dependent on $R_{\rm eq}$. Furthermore, in the steady state, we have $R_{\rm eq} = 8R_{\rm o}/\pi^2$ and the steady-state load voltage is

$$\begin{aligned} \overline{V}_{\rm o} &= \lim_{s\to 0} \frac{1}{C_{\rm f} s + 1/R_{\rm o}} I_{\rm r} = \frac{2}{\pi} \left|\overline{I}_{\rm s}\right| R_{\rm o} \\ &= \frac{2MV_1}{\pi L_{\rm pr}} f(U) \cdot \frac{R_{\rm o}}{R_{\rm eq}} \\ &= \frac{V_{\rm dc} M}{L_{\rm pr}} f(U) \end{aligned} \tag{16}$$

which reveals that the steady-state load voltage is independent of $R_{\rm o}$. Under this consideration, it would be reasonable to neglect dependence variables regarding $R_{\rm o}$ to obtain a simplified version of (11), i.e.,

$$A(p, h_1) V_{\rm o} = B(p) f(U) \tag{17}$$

where $B(p)$ is the same as the one defined in (12a) and

$$A\left(p, h_1\right) = p^{n_a} + \sum_{i=1}^{n_a} \left(a_{i,0} + a_{i,1} h_1\right) p^{n_a - i}. \tag{18}$$

On the other hand, if the output variable is chosen as the load current $I_{\rm o}$, then according to the relation $V_{\rm o} = I_{\rm o} R_{\rm o}$, we have

$$A(p, h_1) I_{\rm o} = B(p, h_2) f(U) \tag{19}$$

where $A(p, h_1)$ is the same as the one defined in (18) and

$$B(p, h_2) = \sum_{i=0}^{n_b} b_i h_2 p^{n_b - i}. \tag{20}$$

Once the model structure has been determined, the unknown model parameters can be estimated from sampled input–output data $\{V_{{\rm o},k}, U_k\}$ and scheduling variables $\{h_{1,k}, \ldots, h_{n_h,k}\}$, $k = 1, ..., N$. For example, in the case of (11), the parameter estimation problem is defined as

$$\widehat{\boldsymbol{\vartheta}} = \arg\min_{\boldsymbol{\vartheta}} \frac{1}{2N} \sum_{k=1}^{N} \left(V_{{\rm o},k} - \widehat{V}_{{\rm o},k}\right)^2 \tag{21}$$

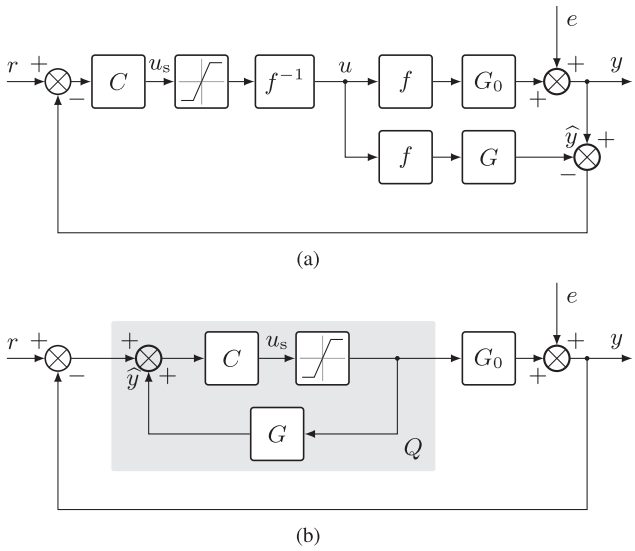

Fig. 2. Basic IMC. (a) Block diagram. (b) Equivalent structure.

where $\widehat{V}_{{\rm o},k}$ is the output generated from the model, and

$$\boldsymbol{\vartheta} = \left[a_{1,0}, \ldots, a_{1,n_h}, a_{2,0}, \ldots, a_{n_a,n_h}, b_0, \ldots, b_{n_b}, c\right]^{\rm T}. \tag{22}$$

The optimization problem (21) can be solved by a standard optimization procedure such as the Gauss–Newton method. To save the space, the detailed algorithm will not be presented here, and the interested reader is directed to references such as [36].

III. Control Design

The IMC was first introduced in [34] and has been widely used in process control, thanks to its robustness against disturbances. The basic IMC is shown in Fig. 2(a), where r is the reference signal, u the actuating signal, f the input nonlinearity, e the disturbance, y the output signal, $\widehat{y}$ the predicted output, C the controller, G_0 the rational part of true plant, and G the rational part of the model. Since the full-bridge inverter introduces a static nonlinearity $f(U)$ to the system and the phase shift is only allowed to be in the interval $[0, \pi]$, a saturation block and linearization block is added to the control loop. After that, the control can be designed following the procedure of linear control design. For convenience in the notation, the input and output variables of the LCC-S WPT system will also be denoted by u and y, respectively. The model $G(p)$ is then formulated as

$$G(p) = \frac{B(p)}{A(p, h_1, h_2, h_3)}. \tag{23}$$

For the basic IMC structure shown in Fig. 2(a), the closed-loop transfer function of the system takes the form

$$\begin{aligned} y = &\frac{G_0(p) C(p)}{1 + \left(G_0(p) - G(p)\right) C(p)} r \\ &+ \frac{1 - G(p) C(p)}{1 + \left(G_0(p) - G(p)\right) C(p)} e. \end{aligned} \tag{24}$$

Fig. 2(a) can also be transformed to the conventional feedback structure shown in Fig. 2(b), where the controller is

$$Q(p) = \frac{C(p)}{1 - G(p)C(p)}. \tag{25}$$

It can be seen from (24) that, in the ideal case where there is no modeling error, i.e., $G(p) = G_0(p)$, the model is invertible, and the control is designed as the inverse model, i.e., $C(p) = 1/G(p)$, we have $y = r$, meaning that the controlled variable tracks perfectly the command input.

In practical situations, although it is possible to use the system identification technique to infer a model that accurately describes the system dynamics, it is not always guaranteed that the model is invertible, due to factors such as pure differentiation, time delay, right-half plane (RHP) zeros, etc. A practical way for control design is as follows. First, the model is decomposed as

$$G(p) = G_{\mathrm{m}}(p)G_{\mathrm{n}}(p) \tag{26}$$

where $G_{\mathrm{m}}(p)$ is the minimum phase part while $G_{\mathrm{n}}(p)$ is non-minimum phase part. Taking $G(p) = (p-4)/(p^2 + 2.8p + 4)$ as an example, the corresponding minimum and nonminimum phase parts are, respectively, $G_{\mathrm{m}}(p) = 1/(p^2 + 2.8p + 4)$ and $G_{\mathrm{n}}(p) = p - 4$. Subsequently, the controller is designed based on the minimum phase part $G_{\mathrm{m}}(p)$ as

$$C(p) = \frac{F(p)}{G_{\mathrm{m}}(p)} = \frac{\lambda^n}{(p+\lambda)^n G_{\mathrm{m}}(p)} \tag{27}$$

where $n \in \mathbb{N}$ is chosen such that $C(p)$ is strictly proper, and $F(p)$ is a low-pass filter with break-point frequency λ. If $G(p) = G_0(p)$, the closed-loop transfer function (24) becomes

$$y = F(p)G_{\mathrm{n}}(p)r + (1 - F(p)G_{\mathrm{n}}(p))e \tag{28}$$

from which it is obvious that $F(p)$ will dominate the reference tracking performance of the closed-loop system.

A. Handling of Rectifier Nonlinearity

The rectifier is a nonlinear element in which the current can only flow from the resonant tank to the load. Due to the existence of dc bias voltage provided by the output filter C_{f}, the rectifier will enter the DCM if the induced voltage at the input port is lower than the load voltage. In the DCM, there is no current flowing through the rectifier, meaning that the system is out of control from the primary side.

To illustrate the above-mentioned problem, let us consider the system presented in Fig. 3. For the full-bridge inverter, an increase in U means less energy to be injected into the resonant tank and, as a result, the induced voltage across the input port of the diode bridge will decrease. If the induced voltage reduces to a value that is smaller than the dc bias voltage V_{o} provided the output filter capacitor C_{f}, the rectifier current will be clamped to zero. In this state, the equivalent resistance of the rectifier load R_{eq} becomes very large, as shown in panel (c) of Fig. 4. Moreover, DCM usually occurs at positive steps of U, and it could also occur at negative steps of U if the system has a strongly oscillatory behavior: the rectifier current may be clamped to zero at the negative oscillation half-cycles.

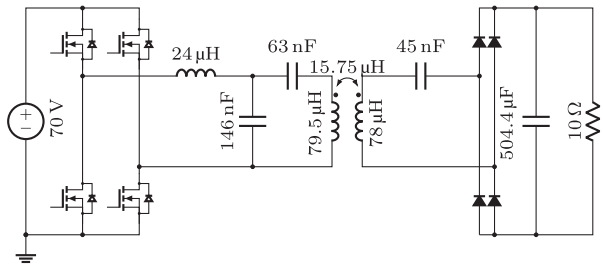

Fig. 3. Main parameters of the simulated system.

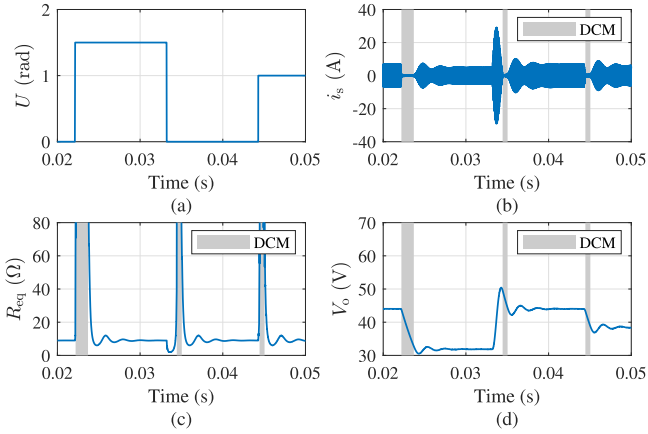

Fig. 4. Dead zones resulted from rectifier bridge.

In DCM, we are not able to regulate the load voltage or current on the primary side. Any inappropriate feedback control would impair the control performance when the system is tentatively uncontrollable. Therefore, it is better to perform open-loop control unless the system has run out of DCM. There remains a question on how to determine the operation mode. Here, a method based on monitoring R_{eq} is proposed: when R_{eq} is larger than a certain threshold, we say that the system is in DCM, and open-loop control is enabled, otherwise when the system is in continuous conduction mode, feedback control is adopted; see the next section for more details.

B. Proposed Control Structure

In this section, we investigate how to implement the control strategy suggested in the previous section. The proposed control structure (see Fig. 5) can be viewed as a modified version of the two degrees of freedom IMC, where a reference filter $F_1(p)$ and a disturbance filter $F_2(p)$ are introduced to separately tune the reference tracking and disturbance rejection performance. The novelty lies in the introduction of the switch S in the feedback channel to switch between open-loop control and closed-loop control. The state of the switch is determined by R_{eq}: when R_{eq} increases to a value larger than the upper bound ν_+, S is switched OFF and open-loop control is enabled; while if R_{eq} drops to a value smaller than the lower bound ν_-, S is switched ON and closed-loop control is enabled.

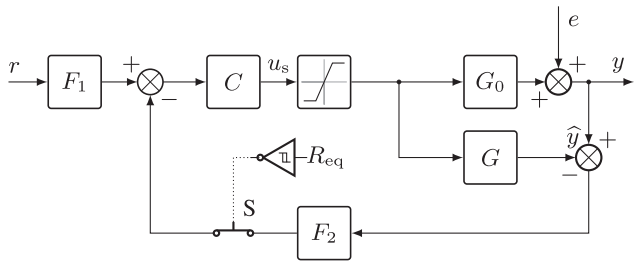

Fig. 5. Proposed two degrees of freedom IMC structure. The states of S is dependent on R_{eq}: if $R_{eq} > \nu_+$, S is switched OFF, while if $R_{eq} < \nu_-$, S is switched ON.

Below is given a discussion on the transfer function when the system is operated in open loop or closed loop. Since the LPV model derived in Section II-B has a scalar numerator, there is no RHP zero in the identified model, i.e., $G_m(p) = G(p)$, and the controller can be designed as $C(p) = F(p)/G(p)$. It is further assumed that the identified model $G(p)$ is accurate, i.e., $G(p) \approx G_0(p)$. Under the above assumptions, when the system is operated in open loop with S being switched OFF, and the open-loop transfer function from r to y takes the form

$$y = F_1(p)C(p)G_0(p)r \approx F(p)F_1(p)r \tag{29}$$

showing that y is able to track r if $F_1(p)F(p)$ is designed to have a unit steady-state gain.

Again, in the closed-loop control scenario when S is switched ON, the transfer function that relates y to r and e becomes

$$\begin{aligned} y &= \frac{G_0(p)C(p)F_1(p)}{1 + (G_0(p) - G(p))\,C(p)F_2(p)}r \\ &\quad + \frac{1 - G(p)C(p)F_2(p)}{1 + (G_0(p) - G(p))\,C(p)F_2(p)}e \\ &\approx F(p)F_1(p)r + (1 - F(p)F_2(p))\,e \end{aligned} \tag{30}$$

from which it is clear that $F_1(p)$ affects the reference tracking performance, while $F_2(p)$ affects the disturbance rejection performance.

IV. Experimental Results

In this section, experiments are carried out to validate the effectiveness of the proposed modeling and control method. The experimental apparatus is shown in Figs. 6 and 7, along with the main circuit component parameters listed in Table I. In these tests, the load resistance is assumed to vary with respect to time in the interval

$$R_o \in [5, 20]\ \Omega. \tag{31}$$

More details regarding the experimental results are shown in the following two sections.

A. Model Identification

The data used for model identification should be sufficiently informative to ensure the identifiablility of the system. To this end, the phase shift of the inverter is chosen as a sequence of uniformly distributed random numbers drawn from the interval $[0, \pi]$ rad. Once the perturbation sequence is applied to inverter, the peak value of the secondary resonant current I_{spk}, the load voltage V_o, and the load current I_o are simultaneously sampled with the sampling interval $T_s = 0.02$ ms, and a total number of $N = 10\,000$ samples are collected. The data are transmitted from the secondary side to the primary controller via wireless communication. The communication delay is about 840 μs.

TABLE I
Main Circuit Parameters

Item	Symbol	Value
Primary series compensation capacitor	C_p	227 nF
Primary parallel compensation capacitor	C_{pr}	312 nF
Secondary series compensation capacitor	C_s	132 nF
Output filter capacitor	C_f	600 μF
Switching frequency	f_0	85 kHz
Self-inductance of the primary coil	L_p	27.2 μH
Primary parallel compensation inductor	L_{pr}	11 μH
Self-inductance of the secondary coil	L_s	27.6 μH
Mutual inductance	M	11.782 μH
Load resistance	R_o	$5 \sim 20\ \Omega$
Communication delay	τ	840 μs
Input dc voltage	V_{dc}	30 V

The phase shift U, load voltage V_o, load current I_o, load resistance R_o, and equivalent rectifier load R_{eq} are shown in Fig. 8, where numerous dead zones can be observed. In steady states, $R_{eq} = 8R_o/\pi^2 \in [4.1, 16.2]\ \Omega$ according to (31). The dead zone shown in Fig. 8 is the interval, where $R_{eq} \geqslant 20\ \Omega$. Interestingly, the rate of V_o changes at falling edges is much slower than that at rising edges.

Subsequently, we identify a second-order model using the method presented in [36, Algorithm 1], where the parameters in denominator polynomial are dependent on three variables $h_1 = R_{eq}$, $h_2 = 1/R_o$, and $h_3 = R_{eq}/R_o$

$$\begin{aligned} V_o &= \widehat{G}(p)\,(\cos(U/2) + \widehat{c}) \\ &= \frac{\widehat{b}\,(\cos(U/2) + \widehat{c})}{p^2 + \sum_{\ell=1}^{3}\left((\widehat{a}_{1,0} + \widehat{a}_{1,\ell}h_\ell)p + \widehat{a}_{2,0} + \widehat{a}_{2,\ell}h_\ell\right)} \end{aligned} \tag{32}$$

with $\widehat{a}_{1,0} = 4.7634 \cdot 10^3$, $\widehat{a}_{1,1} = 1.7310 \cdot 10^3$, $\widehat{a}_{1,2} = 3.1087 \cdot 10^4$, $\widehat{a}_{1,3} = -2.8008 \cdot 10^3$, $\widehat{a}_{2,0} = 1.1674 \cdot 10^7$, $\widehat{a}_{2,1} = -4.5711 \cdot 10^4$, $\widehat{a}_{2,2} = 3.9292 \cdot 10^5$, $\widehat{a}_{2,3} = 3.2361 \cdot 10^6$, $\widehat{b} = 4.5534 \cdot 10^8$, and $\widehat{c} = -7.5495 \cdot 10^{-2}$.

As a comparison, we also identify a second-order model, where h_1 is the only scheduling variable

$$\begin{aligned} V_o &= \widehat{G}(p)\,(\cos(U/2) + \widehat{c}) \\ &= \frac{\widehat{b}\,(\cos(U/2) + \widehat{c})}{p^2 + (\widehat{a}_{1,0} + \widehat{a}_{1,1}h_1)p + \widehat{a}_{2,0} + \widehat{a}_{2,1}h_1} \end{aligned} \tag{33}$$

with $\widehat{a}_{1,0} = 6.1753 \cdot 10^3$, $\widehat{a}_{1,1} = 1.4977 \cdot 10^2$, $\widehat{a}_{2,0} = 1.1944 \cdot 10^7$, $\widehat{a}_{2,1} = -4.3404 \cdot 10^4$, $\widehat{b} = 3.8776 \cdot 10^8$, and $\widehat{c} = -6.0303 \cdot 10^{-2}$.

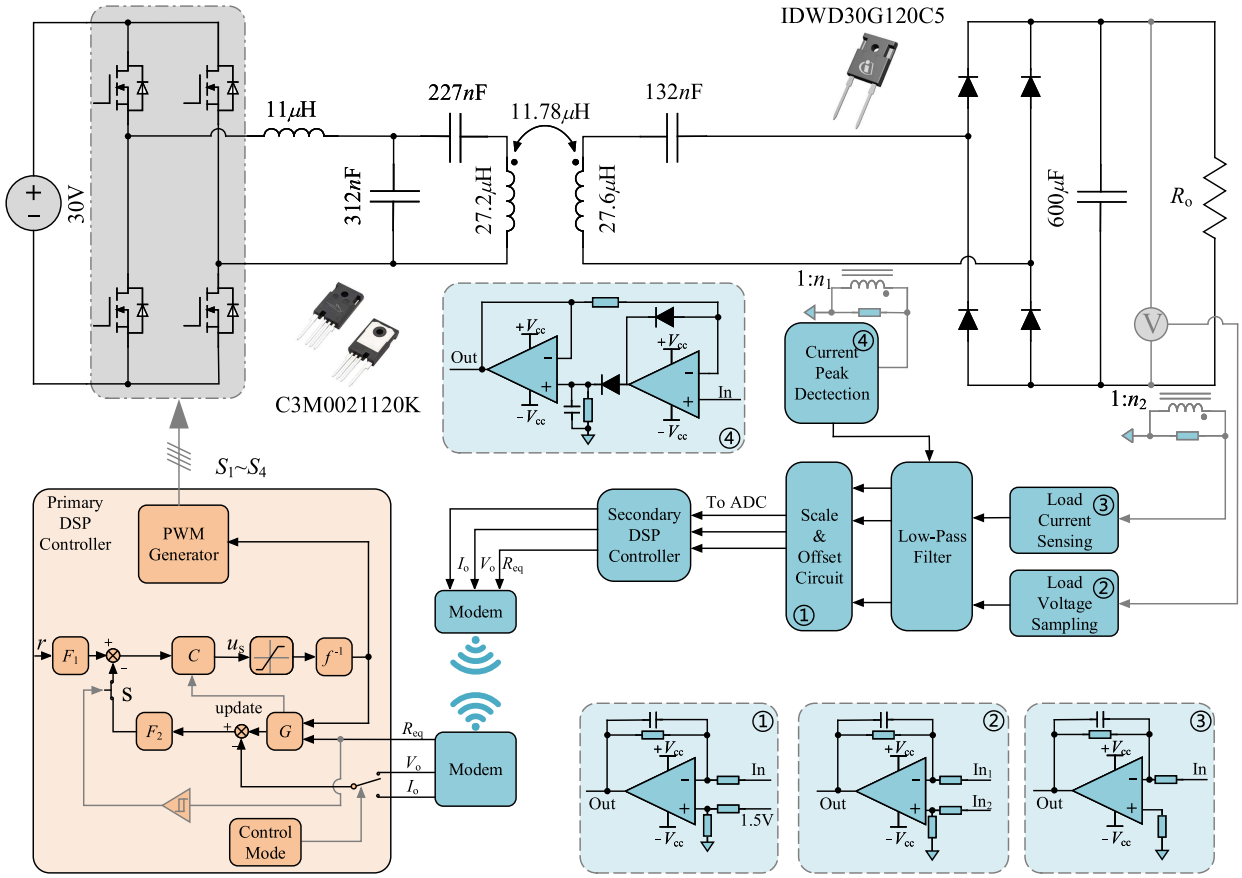

Fig. 6. Detailed explanation of the experimental prototype.

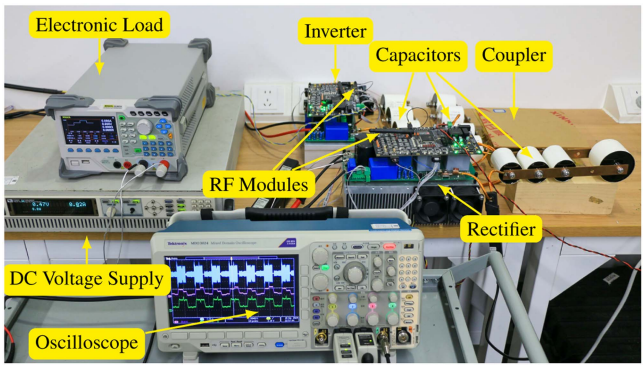

Fig. 7. Experimental prototype.

The accuracy of the identified models are evaluated by the fitness ratio defined below

$$\text{fit} = 1 - \frac{\|V_o - \widehat{V}_o\|}{\|V_o - \text{mean}\{V_o\}\|} \tag{34}$$

where $\widehat{V}_o$ is the predicted output from the identified model. The fitness ratios and predicted outputs of the identified models (32) and (33) are shown in Fig. 9, from which we can see that model (32) yields a higher fitness ratio (fit = 0.9) because its denominator parameters are dependent on all the dependence variables h_1, h_2, and h_3. On the contrary, when we consider the simplified model (33) where the denominator parameters are dependent on only h_1, the model accuracy declines slightly (fit = 0.84). Fortunately, the slight decrease in accuracy does not affect too much output response. From these comparative results, it is then reasonable to design the IMC based on the simpler model (33).

When the output variable is chosen as the load current, by the relation $I_o = V_o/R_o$ and following from (32) and (33), the models that relates I_o and U are immediately obtained as (see Fig. 10 for the model responses)

$$I_o = \frac{\widehat{b}h_2\left(\cos(U/2) + \widehat{c}\right)}{p^2 + \sum_{\ell=1}^{3}\left((\widehat{a}_{1,0} + \widehat{a}_{1,\ell}h_\ell)p + \widehat{a}_{2,0} + \widehat{a}_{2,\ell}h_\ell\right)} \tag{35a}$$

$$I_o = \frac{\widehat{b}h_2\left(\cos(U/2) + \widehat{c}\right)}{p^2 + (\widehat{a}_{1,0} + \widehat{a}_{1,1}h_1)p + \widehat{a}_{2,0} + \widehat{a}_{2,1}h_1} \tag{35b}$$

in which the model parameters are the same than those in models (32) and (33).

B. Control of Load Voltage and Current

In this section, we validate the IMC shown in Fig. 5 for load voltage or current regulation. To achieve fast reference tracking, the reference filter is designed as $F_1(p) = 1$, while

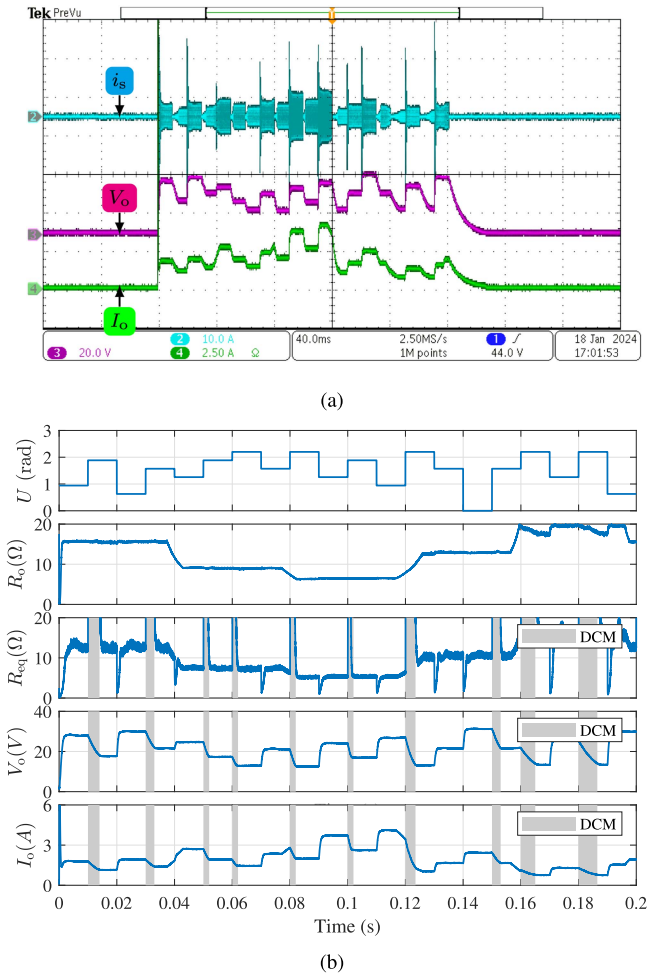

Fig. 8. Experimental data for model identification. (a) Original oscilloscope data. (b) Subsampled data from the oscilloscope data.

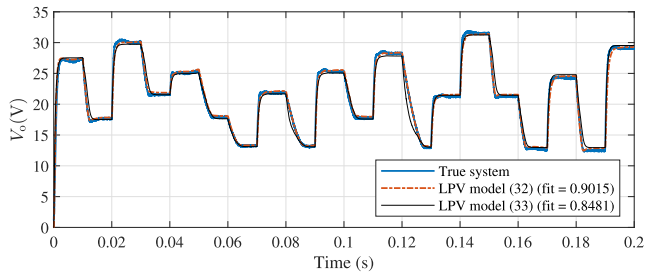

Fig. 9. Prediction of the load voltage using the models in (32) and (33).

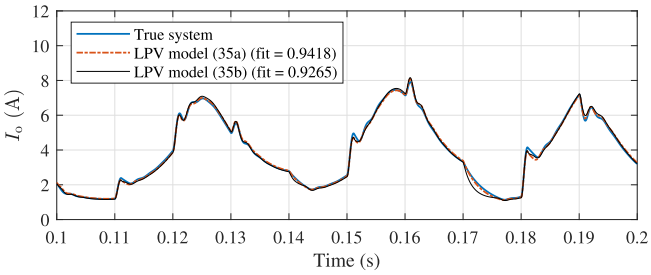

Fig. 10. Prediction of the load current using the models in (35a) and (35b).

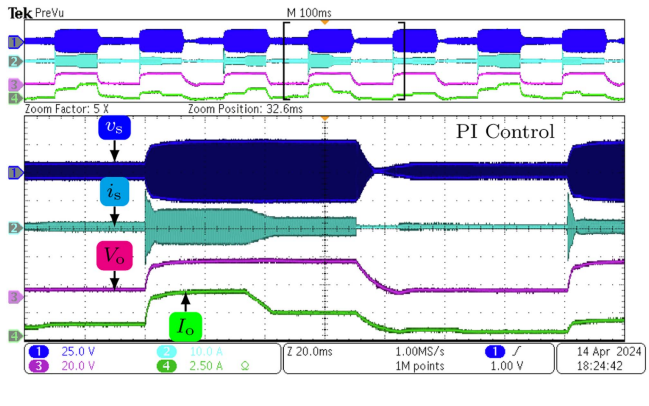

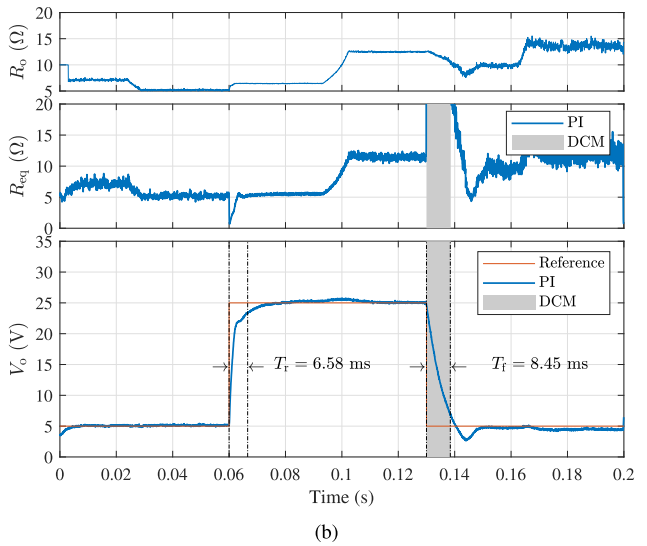

Fig. 11. Load voltage control using PI, where T_r is the rising time when V_o steps from 5 V up to 25 V, while T_f is the falling time when V_o steps from 25 V down to 7 V. (a) Original oscilloscope data. (b) Subsampled data from the oscilloscope data.

the disturbance filter is designed as

$$F_2(p) = \frac{\lambda_2}{p + \lambda_2} \tag{36}$$

where λ_2 is the break-point frequency.

To improve the control performance during DCM, we switch OFF S in Fig. 5 to enable open-loop control if the instantaneous value of R_{eq} is larger than $\nu_+ = 30$, while switch ONS to enable closed-loop control if $R_{eq} < \nu_- = R_o$. We first consider load voltage control, and the simplified model (33) is used for control design. Since the relative order of (33) is 2, the controller $C(p)$ is then designed as

$$\begin{aligned} C(p) &= \frac{F(p)}{\widehat{G}(p)} \\ &= \frac{\lambda^2 \left(p^2 + (\widehat{a}_{1,0} + \widehat{a}_{1,1}h_1)p + \widehat{a}_{2,0} + \widehat{a}_{2,1}h_1\right)}{\widehat{b}(p+\lambda)^2} \end{aligned} \tag{37}$$

where $\widehat{a}_{1,0} = 6.1753 \cdot 10^3, \widehat{a}_{1,1} = 1.4977 \cdot 10^2, \widehat{a}_{2,0} = 1.1944 \cdot 10^7$, $\widehat{a}_{2,1} = -4.3404 \cdot 10^4$, and $\widehat{b} = 3.8776 \cdot 10^8$.

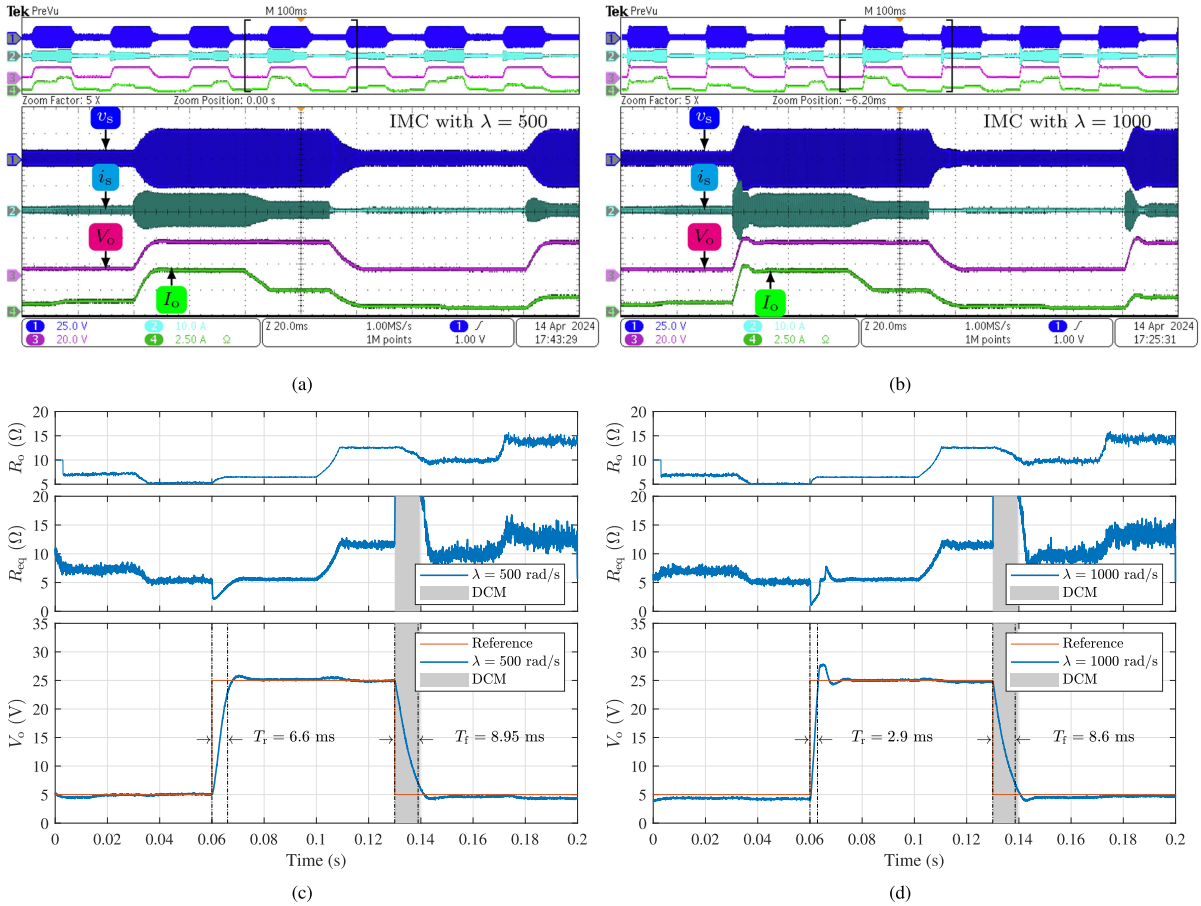

Fig. 12. Load voltage control using IMC ($\lambda = 500$ and 1000 rd/s), where T_r is the rising time when V_o steps from 5 V up to 23 V, while T_f is the falling time when V_o steps from 25 V down to 7 V. (a) and (b) Original oscilloscope data. (c) and (d) Subsampled data from the oscilloscope data.

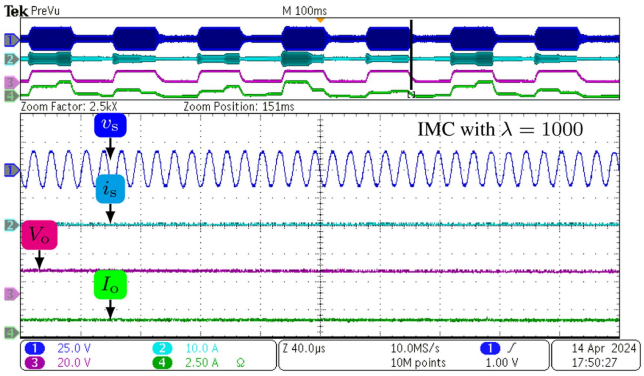

Fig. 13. Zooming part of the DCM in Fig. 12(b).

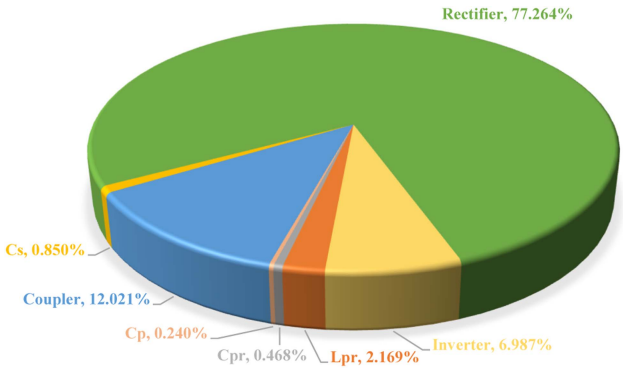

Fig. 14. Power loss distribution.

Here, a question remains to answer is how to choose the parameters λ and λ_2. Some guidelines are suggested in the following:

1) In real applications, disturbances are inevitable due to the existence of measurement noise, discretization errors, model mismatch, etc. The role of $F_2(p)$ is to mitigate the effect of these disturbances in the feedback loop. To preserve the useful information as much as possible, a simple way is to let λ_2 be the bandwidth of $\widehat{G}(p)$. According to (33), the bandwidth of $\widehat{G}(p)$ varies as a function of R_{eq}, and the maximum bandwidth $\lambda_{max} = 2600$ rad/s is obtained at $R_{eq} = 0\ \Omega$. In this regard, we can set $F_2(p) = 3000$ rad/s.
2) When $F_1(p) = 1$, the reference response is dominated by $F(p)$: the larger λ is, the faster the reference response can be. However, λ cannot be chosen arbitrarily large

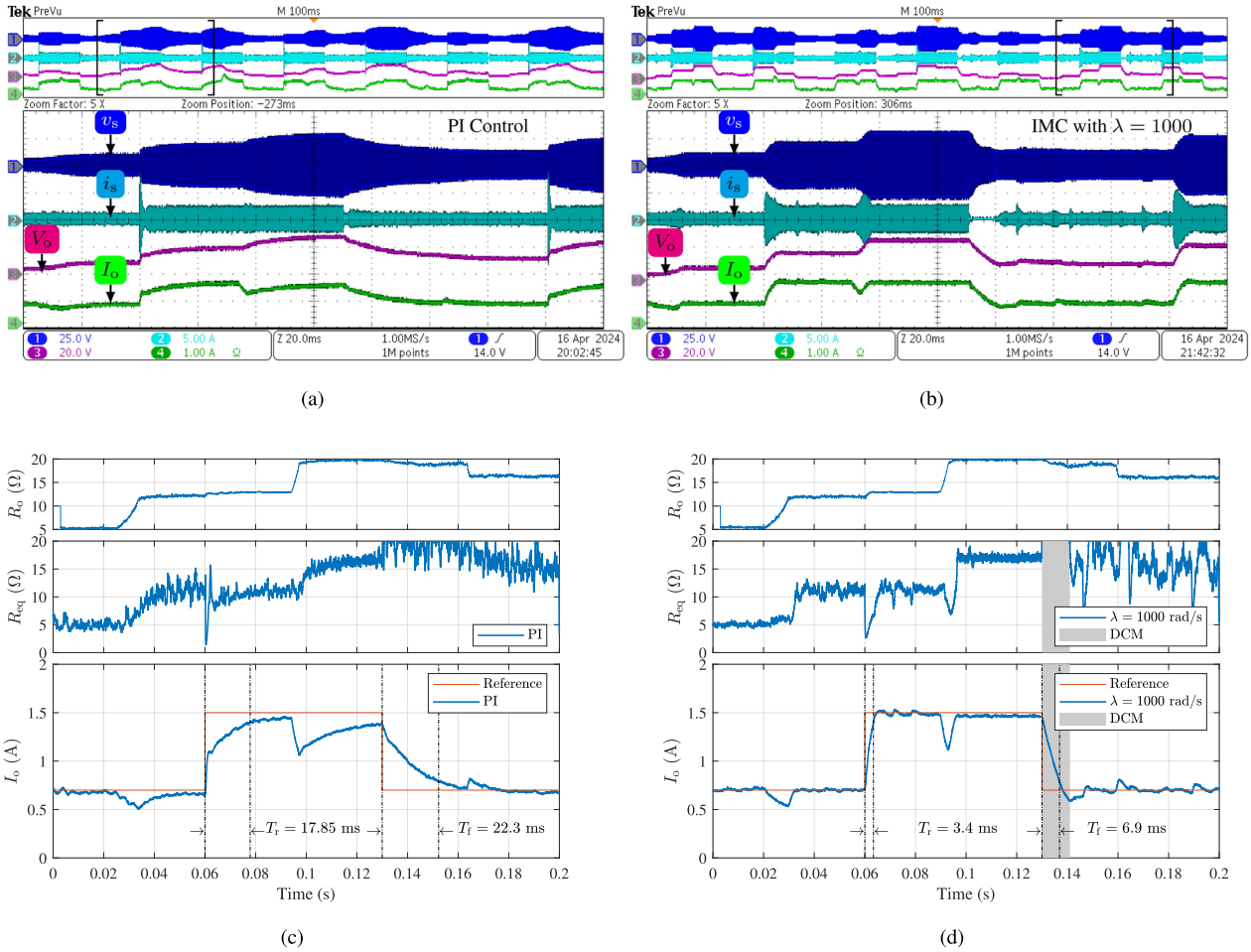

Fig. 15. Load current control using PI and IMC with $\lambda = 1000$ rad/s, where T_r is the rising time when I_o steps from 0.7 A up to 1.42 A, while T_f is the falling time when I_o steps from 1.5 A down to 0.78 A. (a) and (b) Original oscilloscope data. (c) and (d) Subsampled data from the oscilloscope data.

because it will deteriorate robustness of the system to disturbances and lead to overshoots and oscillations in the output response. Therefore, λ should be carefully chosen in order to tradeoff between control quality and robustness. Here, we suggest to tune λ starting from $\lambda_{\max}$ down to a value where satisfactory output response is obtained. In this example, we compare two values for λ: 500 and 1000 rad/s.

The experimental results for load voltage control using proportional integral (PI) control are presented in Fig. 11. The PI parameters are tuned at $R_o = 10\ \Omega$ as $K_p = -0.004$ and $K_i = -7$. This means that the PI control will give the best performance when $R_o = 10\ \Omega$, but the performance decays when the load resistance deviates too far from the nominal value. The experimental results for load voltage control using IMC are available in Fig. 12.

When the reference r steps from 5 to 25 V at $t = 60$ ms, the load voltage tracks quicker the reference for $\lambda = 1000$ rad/s: the rising time is only $t_r = 2.9$ ms (here t_r is the time consumption when the output reaches 90% the change of reference), while this value for $\lambda = 500$ rad/s is 6.6 ms. However, the load voltage has an obvious overshoot when $\lambda = 1000$ rad/s, which means that the closed-loop system is not as robust as the case with $\lambda = 500$ rad/s. This phenomenon coincides the argument that λ enables us to choose between control quality and robustness. When the reference steps from 25 down to 5 V at $t = 130$ ms, the system enters immediately DCM and, after that, takes about 9 ms to recover from this state (see Fig. 13 for a zooming part of the DCM). In this case, the switch S in Fig. 5 is switched OFF so that the system is operated in open loop. At time $t = 140$ ms, the system runs out of the DCM state, then S is switched ON to enable closed-loop control. Due to the presence of DCM, the system takes much longer time to converge for negative steps of the reference (the falling time is $t_f = 8.6$ ms for $\lambda = 1000$ rad/s). It can be seen that the performance of the PI controller at the falling edge of the load voltage is not so satisfactory, because the control action is imposed during DCM but the load voltage is actually not controllable at this time. This problem does not happen in the proposed IMC, because the control system will switch to open loop if DCM is detected.

Subsequently, let us consider load current control. Since $I_o = V_o/R_o$, the same control setting in load voltage control can be used for load current control, except for the controller $C(p)$,

which is designed based on the identified model (35b) as

$$C(p) = \frac{F(p)}{\widehat{G}(p)} = \frac{\lambda^2\left(p^2 + (\widehat{a}_{1,0} + \widehat{a}_{1,1}h_1)p + \widehat{a}_{2,0} + \widehat{a}_{2,1}h_1\right)}{\widehat{b}h_2(p+\lambda)^2}. \quad (38)$$

The experimental results are shown in Fig. 15. It seems that the load current responses resembles the load voltage responses shown in Fig. 11. However, a small flaw that can be observed from Fig. 15 is the spikes when the load resistance changes at $t \approx 25$, 95, and 165 ms. The reason could be explained as follows: the LCC-S WPT system acts like a voltage source, i.e., the load voltage remains quasi-constant in the presence of load variation, so forcing the load current to change when load resistance changes.

Finally, let us present the efficiency of the system. When the load is fixed as 5 Ω, the measured input power of the system is $P_{\text{in}} = 139$ W, while the measured output power is approximately 122.77 W, so the efficiency of the system is 88.3%. This efficiency can be further improved if the power level becomes higher. The power loss distribution is presented in Fig. 14.

V. Conclusion

This article has addressed the problem of modeling and control for an LCC-S WPT system. Due to the constant voltage output property of the LCC-S WPT system, various dead zones can arise in the rectifier current during the load voltage/current regulation process. Also, the load resistance could change with respect to time, forcing the load current to change. In this article, an LPV model is proposed to provide a better explanation into the dead-zone and load variation nonlinearities. Based on the identified LPV model, a modified two degrees of freedom IMC structure is proposed for load voltage/current control. The proposed structure can switch adaptively between open loop and closed loop: when a dead zone arises, the load voltage/current is uncontrollable from the primary side and so the system is switched to open-loop mode; once the system has run out of this dead zone, the system is switched back to closed-loop mode. Experimental results have shown that the proposed LPV models are quite efficient and accurate in the presence of numerous dead zones and moderate load variation, and in the proposed IMC-based structure, the open- and closed-loop switching mechanism achieves very good reference tracking performance in both load voltage control and load current control.

References

[1] L. Zhao, D. J. Thrimawithana, and U. K. Madawala, "Hybrid bidirectional wireless EV charging system tolerant to pad misalignment," *IEEE Trans. Ind. Electron.*, vol. 64, no. 9, pp. 7079–7086, Sep. 2017.

[2] S. Li and C. C. Mi, "Wireless power transfer for electric vehicle applications," *IEEE Trans. Emerg. Sel. Topics Power Electron.*, vol. 3, no. 1, pp. 4–17, Mar. 2015.

[3] S. Y. R. Hui, W. Zhong, and C. K. Lee, "A critical review of recent progress in mid-range wireless power transfer," *IEEE Trans. Power Electron.*, vol. 29, no. 9, pp. 4500–4511, Sep. 2014.

[4] Z. Zhang, H. Pang, A. Georgiadis, and C. Cecati, "Wireless power transfer–An overview," *IEEE Trans. Ind. Electron.*, vol. 66, no. 2, pp. 1044–1058, Feb. 2019.

[5] Z. Li, C. Zhu, J. Jiang, K. Song, and G. Wei, "A 3-kW wireless power transfer system for sightseeing car supercapacitor charge," *IEEE Trans. Power Electron.*, vol. 32, no. 5, pp. 3301–3316, May 2017.

[6] W. Zhou, L. Huang, B. Luo, R. Mai, Z. He, and A. P. Hu, "A general mutual coupling model of MIMO capacitive coupling interface with arbitrary number of ports," *IEEE Trans. Power Electron.*, vol. 36, no. 6, pp. 6163–6167, Jun. 2021.

[7] H. Hu, S. Duan, T. Cai, and P. Zheng, "A current-sharing compensation method for high-power-medium-frequency coils composed of multiple branches connected in parallel," *IEEE Trans. Ind. Electron.*, vol. 69, no. 5, pp. 4637–4651, May 2022.

[8] Z. Liu, Y.-G. Su, Y.-M. Zhao, A. P. Hu, and X. Dai, "Capacitive power transfer system with double t-type resonant network for mobile devices charging/supply," *IEEE Trans. Power Electron.*, vol. 37, no. 2, pp. 2394–2403, Feb. 2022.

[9] Y. Fan, Y. Sun, X. Dai, Z. Zuo, and A. You, "Simultaneous wireless power transfer and full-duplex communication with a single coupling interface," *IEEE Trans. Power Electron.*, vol. 36, no. 6, pp. 6313–6322, Jun. 2021.

[10] P. Deng, C. Tang, Y. Fan, M. Sun, Z. Liu, and X. Li, "A frequency regulation strategy for dynamic process noise suppression in LCC-S WPT systems," *IEEE Trans. Power Electron.*, vol. 37, no. 11, pp. 13978–13988, Nov. 2022.

[11] Y. Chen et al., "A clamp circuit-based inductive power transfer system with reconfigurable rectifier tolerating extensive coupling variations," *IEEE Trans. Power Electron.*, vol. 39, no. 2, pp. 1942–1946, Feb. 2024.

[12] T. Feng, Z. Zuo, Y. Sun, X. Dai, X. Wu, and L. Zhu, "A reticulated planar transmitter using a three-dimensional rotating magnetic field for free-positioning omnidirectional wireless power transfer," *IEEE Trans. Power Electron.*, vol. 37, no. 8, pp. 9999–10015, Aug. 2022.

[13] J. Wu, X. Dai, R. Gao, and J. Jiang, "A coupling mechanism with multidegree freedom for bidirectional multistage WPT system," *IEEE Trans. Power Electron.*, vol. 36, no. 2, pp. 1376–1387, Feb. 2021.

[14] C. Rong, X. He, Y. Zeng, C. Lu, and M. Liu, "High-efficiency orientation insensitive WPT systems using magnetic dipole coil for low-power devices," *IEEE Trans. Power Electron.*, vol. 37, no. 5, pp. 4985–4990, May 2022.

[15] J.-G. Kim, G. Wei, M.-H. Kim, J.-Y. Jong, and C. Zhu, "A comprehensive study on composite resonant circuit-based wireless power transfer systems," *IEEE Trans. Ind. Electron.*, vol. 65, no. 6, pp. 4670–4680, Jun. 2018.

[16] M. Ishihara, K. Umetani, and E. Hiraki, "Strategy of topology selection based on quasi-duality between series–series and series-parallel topologies of resonant inductive coupling wireless power transfer systems," *IEEE Trans. Power Electron.*, vol. 35, no. 7, pp. 6785–6798, Jul. 2020.

[17] X. Hou, H. Hu, Y. Su, Z. Liu, Z. Deng, and R. Deng, "A multirelay wireless power transfer system with double-sided LCC compensation network for online monitoring equipment," *IEEE Trans. Emerg. Sel. Topics Power Electron.*, vol. 11, no. 1, pp. 1262–1271, Feb. 2023.

[18] Z.-J. Liao, Y. Sun, Z.-H. Ye, C.-S. Tang, and P.-Y. Wang, "Resonant analysis of magnetic coupling wireless power transfer systems," *IEEE Trans. Power Electron.*, vol. 34, no. 6, pp. 5513–5523, Jun. 2019.

[19] Y. Zhang and Z. Zhao, "Frequency splitting analysis of two-coil resonant wireless power transfer," *IEEE Antennas Wireless Propag. Lett.*, vol. 13, pp. 400–402, 2014.

[20] A. P. Sample, D. A. Meyer, and J. R. Smith, "Analysis, experimental results, and range adaptation of magnetically coupled resonators for wireless power transfer," *IEEE Trans. Ind. Electron.*, vol. 58, no. 2, pp. 544–554, Feb. 2011.

[21] F. Chen, H. Garnier, Q. Deng, M. K. Kazimierczuk, and X. Zhuan, "Control-oriented modeling of wireless power transfer systems with phase-shift control," *IEEE Trans. Power Electron.*, vol. 35, no. 2, pp. 2119–2134, Feb. 2020.

[22] Z. Huang, S.-C. Wong, and C. K. Tse, "Control design for optimizing efficiency in inductive power transfer systems," *IEEE Trans. Power Electron.*, vol. 33, no. 5, pp. 4523–4534, May 2018.

[23] C. Zhu and W. Zhong, "Small-signal modeling and decoupling control method of modular WPT systems," *IEEE Trans. Power Electron.*, vol. 38, no. 6, pp. 7863–7876, Jun. 2023.

[24] T. Tan, K. Chen, Q. Lin, Y. Jiang, L. Yuan, and Z. Zhao, "Impedance shaping control strategy for wireless power transfer system based on dynamic small-signal analysis," *IEEE Trans. Circuits Syst. I: Regular Papers*, vol. 68, no. 3, pp. 1354–1365, Mar. 2021.

[25] H. Li, J. Xu, F. Gao, Y. Zhang, X. Yang, and H. Tang, "Duty cycle control strategy for dual-side LCC resonant converter in wireless power transfer systems," *IEEE Trans. Transport. Electrific.*, vol. 8, no. 2, pp. 1944–1955, Jun. 2022.
[26] H. Li, J. Fang, and Y. Tang, "Dynamic phasor-based reduced-order models of wireless power transfer systems," *IEEE Trans. Power Electron.*, vol. 34, no. 11, pp. 11361–11370, Nov. 2019.
[27] C. Qi, G. Zheng, Y. Liu, J. Liang, H. Wang, and M. Fu, "A simplified three-order small-signal model for capacitive power transfer system using series compensation," *IEEE Trans. Power Electron.*, vol. 38, no. 5, pp. 5688–5692, May 2023.
[28] H. Feng and S. M. Lukic, "Reduced-order modeling and design of single-stage LCL compensated IPT system for low voltage vehicle charging applications," *IEEE Trans. Veh. Technol.*, vol. 69, no. 4, pp. 3728–3739, Apr. 2020.
[29] F. Chen, Z. Deng, H. Hu, and Y. Sun, "Dynamic reduced-order modeling of wireless power transfer systems via polynomial approximation," *IEEE Trans. Power Electron.*, vol. 37, no. 7, pp. 7540–7547, Jul. 2022.
[30] M. J. Neath, A. K. Swain, U. K. Madawala, and D. J. Thrimawithana, "An optimal PID controller for a bidirectional inductive power transfer system using multiobjective genetic algorithm," *IEEE Trans. Power Electron.*, vol. 29, no. 3, pp. 1523–1531, Mar. 2014.
[31] Z. Zhou, L. Zhang, Z. Liu, Q. Chen, R. Long, and H. Su, "Model predictive control for the receiving-side DC–DC converter of dynamic wireless power transfer," *IEEE Trans. Power Electron.*, vol. 35, no. 9, pp. 8985–8997, Sep. 2020.
[32] C. Xia, W. Wang, G. Chen, X. Wu, S. Zhou, and Y. Sun, "Robust control for the relay ICPT system under external disturbance and parametric uncertainty," *IEEE Trans. Control Syst. Technol.*, vol. 25, no. 6, pp. 2168–2175, Nov. 2017.
[33] R. W. Erickson and D. Maksimovic, *Fundamentals of Power Electronics*. New York, NY, USA: Springer Science & Business Media, 2007.
[34] C. E. Garcia and M. Morari, "Internal model control. A unifying review and some new results," *Ind. Eng. Chem. Process Des. Develop.*, vol. 21, no. 2, pp. 308–323, 1982.
[35] S. Zhao, C. Tang, F. Chen, D. Zhao, P. Deng, and J. Xiao, "Modeling and control of the WPT system subject to input nonlinearity and communication delay," *IEEE Trans. Power Electron.*, vol. 38, no. 11, pp. 14776–14787, Nov. 2023.
[36] F. Chen, H. Hu, L. Zhao, A. Padilla, and J. Hou, "A linear parameter varying Hammerstein model for dynamic modeling of WPT systems," *IEEE Trans. Power Electron.*, vol. 38, no. 12, pp. 16230–16244, Dec. 2023.
[37] S. Ladan and K. Wu, "Nonlinear modeling and harmonic recycling of millimeter-wave rectifier circuit," *IEEE Trans. Microw. Theory Techn.*, vol. 63, no. 3, pp. 937–944, Mar. 2015.
[38] J. Sun and K. J. Karimi, "Small-signal input impedance modeling of line-frequency rectifiers," *IEEE Trans. Aerosp. Electron. Syst.*, vol. 44, no. 4, pp. 1489–1497, Oct. 2008.
[39] M. Fu, Z. Tang, and C. Ma, "Analysis and optimized design of compensation capacitors for a megahertz WPT system using full-bridge rectifier," *IEEE Trans. Ind. Inform.*, vol. 15, no. 1, pp. 95–104, Jan. 2019.
[40] M. R. Hans and G. M. Gaikwad, "Analysis of rectifier load for electric vehicle wireless charging system," in *Proc. Int. Conf. Smart Electron. Commun.*, 2020, pp. 1095–1098.
[41] J. Sun, J. Cho, A. Huang, H. Kim, and J. Fan, "Accurate rectifier characterization and improved modeling of constant power load wireless power transfer systems," *IEEE Trans. Power Electron.*, vol. 35, no. 8, pp. 7840–7852, Aug. 2020.
[42] Y. Yang, "Precise modeling of nonlinear rectifier loads in wireless power transfer systems," *IEEE Trans. Emerg. Sel. Topics Power Electron.*, vol. 11, no. 3, pp. 3574–3585, Jun. 2023.
[43] I. Batarseh and C. Lee, "High-frequency high-order parallel resonant converter," *IEEE Trans. Ind. Electron.*, vol. 36, no. 4, pp. 485–498, Nov. 1989.

Yuchen Feng (Student Member, IEEE) received the B.Eng. degree in automation in 2018 from the School of Automation, Chongqing University, Chongqing, China, where he is currently working toward the Ph.D. degree in control theory and control engineering.

His current research interests include wireless power transfer and power electronics.

Fengwei Chen was born in Chongqing, China. He received the B.Eng. degree in automation and the M.Eng. degree in control theory and control engineering from Wuhan University, Wuhan, China, in 2009 and 2011, respectively, and the Ph.D. degree in automatic control from the Université de Lorraine, Nancy, France, in 2014.

From 2015 to 2016, he was a Lecturer with the Dalian University of Technology, Dalian, China. From 2017 to 2020, he was an Associate Researcher with Wuhan University, Wuhan, China. Since 2021, he has been with Chongqing University, Chongqing, China, where he is currently an Associate Professor. His research interests include system identification and parameter estimation, with applications to wireless power transfer.

Yue Sun received the B.Eng. degree in electrical engineering, the M.Eng. degree in industrial automation, and the Ph.D. degree in mechanical electrical integrated manufacturing from Chongqing University, Chongqing, China, in 1982, 1988, and 1995, respectively.

He was a Senior Visiting Scholar with the University of Valenciennes, Famars, France, in 1997. He is currently a Professor with the College of Automation, Chongqing University, China. His current research interests include automatic control, wireless power transfer, and power electronics applications.

Tao Lin received the B.Eng. degree in measurement and control technology and instrument from Nanjing Forestry University, Nanjing, China, in 2018. He is currently working toward the Ph.D. degree in control science and engineering with the School of Automation, Chongqing University, Chongqing, China.

His current research interests include bidirectional power transfer and nonlinear modeling.

Fanbin Meng (Student Member, IEEE) received the B.Eng. degree in automation from Chongqing University, Chongqing, China, in 2022. He is currently working toward the M.Eng. degree in control theory and control engineering with Chongqing University, Chongqing, China.

His current research interests include bidirectional wireless power transfer and power electronics.

Hongsheng Hu (Member, IEEE) received the B.Eng. degree in electrical engineering and automation and the Ph.D. degree in power electronics and power drives from the Huazhong University of Science and Technology, Wuhan, China, in 2014 and 2021, respectively.

He is currently an Associate Professor with the School of Automation, Chongqing University, Chongqing, China. His research interests include modularized IPT systems, bidirectional IPT systems, capacitive IPT systems, and power electronics.